Available online at www.sciencedirect.com

jmr&t Journal of Materials Research and Technology

journal homepage: www.elsevier.com/locate/jmrt

Original Article

On the fatigue and dwell-fatigue behavior of a low-density steel and the correlated microstructure origin of damage mechanism

A. Moshiri [a], A. Zarei-Hanzaki [a,**], A.S. Anousheh [a], H.R. Abedi [b,*], Seok Su Sohn [c], Junha Yang [d], M. Jaskari [e], L.P. Karjalainen [f], F. Berto [g]

[a] Hot Deformation and Thermomechanical Processing Laboratory of High Performance Engineering Materials, School of Metallurgy and Materials Engineering, College of Engineering, University of Tehran, Tehran, Iran
[b] School of Metallurgy & Materials Engineering, Iran University of Science and Technology (IUST), Tehran, Iran
[c] Department of Material Science and Engineering, Korea University, 145 Anam-Ro, Seongbuk-Gu, Seoul, 02841, Republic of Korea
[d] Center for High Entropy Alloys, Pohang University of Science and Technology, Pohang, 37673, Republic of Korea
[e] Kerttu Saalasti Institute, Future Manufacturing Technologies Group, University of Oulu, Pajatie 5, Nivala, FI-85500, Finland
[f] Centre for Advanced Steels Research, Materials and Mechanical Engineering Unit, University of Oulu, Oulu, Finland
[g] Department of Mechanical and Industrial Engineering, Norwegian University of Science and Technology, Trondheim, 7491, Norway

ARTICLE INFO

Article history:
Received 24 May 2021
Accepted 29 October 2021
Available online 9 November 2021

Keywords:
Dynamic strain aging
Cyclic deformation
Dwell-fatigue
Low-density steel
Fractography
Damage mechanism

ABSTRACT

The present work deals with revealing the fatigue and dwell-fatigue behavior and correlated damage mechanisms of Fe–Mn–Al–C lightweight steel. Surprisingly, alteration in loading mode from monotonic to cyclic induces reversible dislocation movement and facilitates the occurrence of dynamic strain aging. Additionally, applying dwell time by an acceleration of strain aging intensified stress asymmetry during dwell fatigue. The occurrence of strain aging has a bilateral effect on the crack initiation and growth. On one hand, strain aging stimulates twin formation and retards fatigue crack initiation, however, on the other hand, reduces hardening capacity, restricts the plastic deformation and facilitates crack propagation.

* Corresponding author.
** Corresponding author.
E-mail addresses: zareih@ut.ac.ir (A. Zarei-Hanzaki), habedi@iust.ac.it (H.R. Abedi).
https://doi.org/10.1016/j.jmrt.2021.10.135

1. Introduction

The Fe–Mn–Al–C steels, which have been known as lightweight steels or low-density steels, were previously developed as a replacement for Fe–Cr–Ni steels. The outstanding combination of strength and ductility along with the high specific strength (strength to weight ratio) of lightweight steels candidate these specific groups as a promising choice for industrial applications [1–4]. Various novel dislocation-based deformation mechanisms such as micro-band induced plasticity (MBIP) [5], dynamic slip band refinement (DSBR) [6], and shear band induced plasticity (SIP) [7], have been introduced as the main mechanism responsible for outstanding performance of the lightweight steels. Interestingly, in spite of their high stacking fault energy (SFE) due to the addition of Al to the composition of high-Mn austenitic steels, activation of twinning induced plasticity (TWIP) and transformation induced plasticity (TRIP) effects have been also reported in the course of room temperature monotonic loading [8–12].

It has been well established that the dislocation maneuverability and quality of dislocation movement during cyclic loading are completely different compared with those found in monotonic loading. The concept of reversible dislocation movement has been well described previously [13–18], which may effectively impress activity of the dislocation-based phenomena [19–27]. Anoushe et al. [21] have demonstrated that reversal dislocation path would facilitate the interaction of dislocations and therefore promotes substructure development even in low SFE materials. Nandy et al. [28] have discussed that the reversible strain path can provoke dynamic formation/dynamic dissolution of precipitates through accelerating dislocation–dislocation and dislocation–precipitates interactions. In line to these efforts, it has been illustrated that the reversible dislocation movement could facilitate martensitic transformation and its dynamic reversion into the nano-twinned austenite even at low strain amplitudes [20]. Having all of these researches into the consideration, the present authors came to believe that the alteration in loading mode from monotonic to cyclic would effectively influence the dominant deformation and correlated damage mechanisms. Despite the valuable efforts on unveiling the overlooked mechanisms of strain accommodation under uniaxial loading, to the best of authors' knowledge, there is no comprehensive and systematic study concerning the fatigue properties of lightweight steels. Additionally, it was frequently observed that a significant reduction in fatigue life occurs in many industrial components (e.g., landing gears and turbine engines) exposed to constant high stress for a period known as "dwell time." Detailed examination of the material's behavior during dwell fatigue demonstrates that various vital factors affect the components' lifetime, which is impossible to address during conventional fatigue [29–31]. Despite this essential challenge, the response of lightweight steels to the dwell fatigue has not been studied before.

The present study deals with investigating the room-temperature fatigue behavior of a lightweight steel. This will be supported proposing a newly developed method derived from merging the dwell-fatigue with stress relaxation to assess the involved deformation mechanism. In fact, assessment of dislocation response to the cyclic loading and its contribution to the fatigue performance conventionally (though in-situ characterization) looks impossible. In this respect, the stress relaxation technique has been applied during dwell time in dwell-fatigue loading and considering the time dependency of dislocation movement, the quantity and quality of which has been studied. The current work also tries to unveil the differences between the material responses to the cyclic and monotonic loading. The correlation of the activated deformation mechanisms, damage mechanisms and crack growth behavior has been also addressed.

2. Material and experimental procedures

2.1. Alloy preparation

An austenite-based duplex lightweight steel with a chemical composition of Fe-17.5Mn-8.3Al-0.74C-0.14Si (wt.%) was received in as electro-slag remelted condition to minimize the impurity level. The cast structure was homogenized at 1200 °C for 2 h to eliminate any possibility of macro-segregation and then was hot rolled at the temperature range of 1200–1100 °C followed by the air cooling to break through the cast structure. Subsequently, the short time annealing was accomplished at 1100 °C for 10 min as a solution treatment to obtain a dilute solid solution dual phase microstructure. The SFE of the austenite phase at the room temperature falls into the range of ~85–90 mJ/m^2 which was calculated using the proposed models by Curtze [32] and Saeed-Akbari [33]. Additionally, the apparent density of this material is 6.8 g cm^{-3}, which has been measured using Mettler-Toledo XP205, Mettler-Toledo AG.

2.2. Mechanical testing and sample preparation

2.2.1. Tensile and stress relaxation tests

The room-temperature flow behavior as well as strain rate sensitivity (SRS) of the material was examined using the uniaxial tensile tests under the various strain rates of 0.1, 0.01, 0.001 and 0.0001 s^{-1} at the room temperature. In addition, the stress relaxation tests were performed to investigate the dislocation response to monotonic deformation. In this regard, the specimens were strained up to the true strains of 0.1 and 0.4 with a strain rate of 0.0001 s^{-1}, then the tests were interrupted and held under constant strain for 60 s. Afterward, the samples were strained to the same stress level as the beginning of the last holding time; this procedure as one cycle was repeated five times. Tensile and stress relaxation tests were carried out with Gotech™ AI-7000 LA 30 universal testing machine equipped with a contact extensometer using ASTM standard E8 tensile sample with a gauge length of 25 mm and a sample thickness of 1 mm [34]. All the samples were subjected to the surface grinding and subsequent mirror-polishing to eliminate the effect of surface roughness.

2.2.2. Conventional and dwell fatigue tests

The room-temperature cyclic deformation behavior of the experimental material has been evaluated using fully reversal ($R = -1$) strain-controlled push–pull fatigue test at different strain amplitudes of 0.01, 0.016, 0.02, 0.03 and 0.04, with the

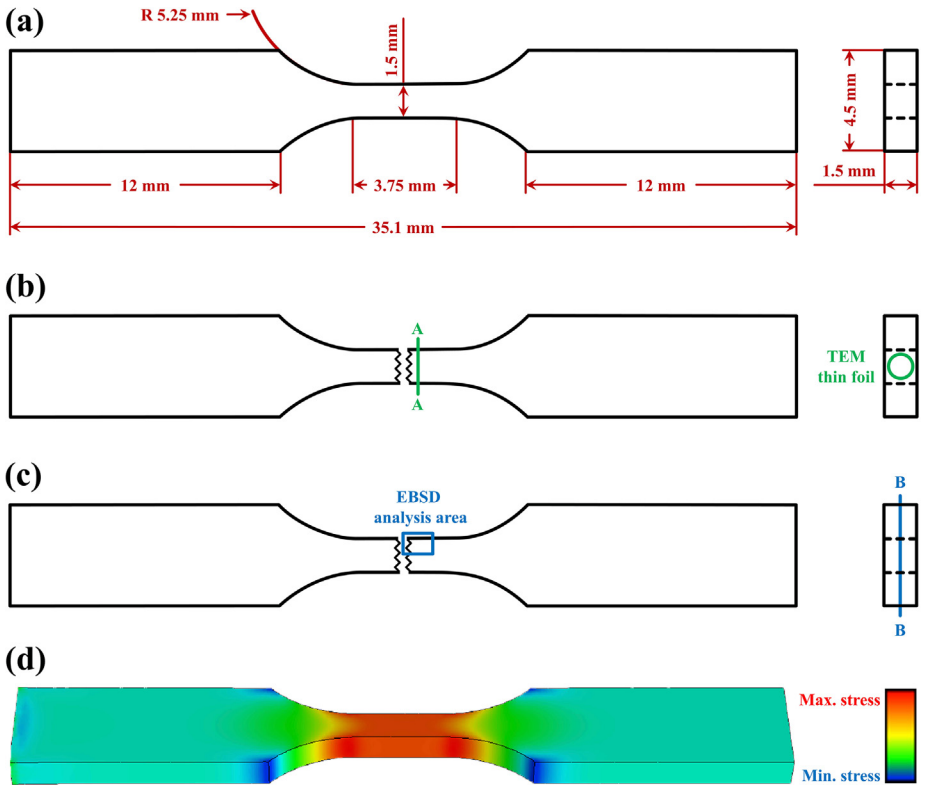

Fig. 1 – (a) The schematic sketch of push–pull fatigue specimen at the top and right view; the position of (b) electron back-scatter diffraction (EBSD) and (c) transmission electron microscopy (TEM) samples on the fractured push–pull fatigue specimen. The EBSD analysis have been performed on the cross-sectional view of the fatigue sample near the fractured surface and A–A line represents the cross-section direction of fractured specimen. B–B line shows the closest region to the fracture surface used for cylindrical TEM thin foil preparation which has been illustrated at the right view; (d) the contour plot of von-Mises stress for the push–pull specimen under tensile/compressive half-cycle.

strain rate ($\dot{\varepsilon}$) of 0.1 s^{-1} and in a triangular waveform. To study the strain aging behavior, the material was also subjected to the cyclic loading with the strain amplitude of 0.04 and different strain rates of 0.07 and 0.02 s^{-1}.

Dwell-fatigue tests were used to well trace the deformation mechanism of cyclic deformation by employing the stress relaxation technique. In this regard, 20, 40, and 60 s dwell times were applied to the maximum and minimum strains of above-mentioned conventional fatigue test with the strain amplitude of 0.04 and the strain rate of 0.1 s^{-1}. The geometry of the push–pull flat fatigue specimen has been demonstrated in Fig. 1(a) which designed based on ASTM standard E606 [35]. To reduce any possibility of surface roughness and stress concentration, the surface grinding followed by mirror-polishing were utilized. All cyclic loading tests were executed using Santam™ STM-50 universal testing machine equipped with a contact extensometer. It is worth mentioning that in order to increase the reliability of the reported results, all test conditions were repeated at least 3 times and the averages of the outcomes were reported.

2.3. *Fractography and microstructural analysis*

The fractography analysis was carried out by the field emission scanning electron microscopy (Fe-SEM) technique, using FEI Nova Nano-SEM™ 450 in secondary electron (SE) mode on the ultrasonically cleaned samples in ethanol for 15 min followed by air drying. The electron back-scatter diffraction (EBSD) analysis with the step size of 200 nm and high-resolution electron back-scatter diffraction (HR-EBSD) analysis with the step size of 50 nm were used to investigate the fatigue crack propagation behavior and to analyze the microstructural evolution around the crack tip. For this aim, the fatigued specimens were cut through the A–A line (as marked in Fig. 1(b)) from near the fracture surface to provide EBSD samples. The cross-sectional views of these samples were prepared by grinding and polishing with 1 μm diamond suspension followed by OP-S suspension for 30 min. EBSD analysis was performed using the CrystAlign system with an EBSD (e-FlashHR, Bruker, Germany) mounted on a field emission gun SEM (S-4300SE, Hitachi, Japan) at a 20 kV acceleration voltage with 4 nA probe current. The data were processed via TSL-OIM software (version 7). Transmission electron microscopy (TEM) analysis was performed using a JEOL JEM-2200FS STEM instrument at 200 kV on the thin film provided from the nearest region to the fractured surface (as marked in Fig. 1(c) by B–B line) to be representative for the maximum applied stress region (Fig. 1(d)). Moreover, in order to demonstrate phase fraction of the initial microstructure, a Ferritescope (Fischer MP30) instrument accompanied with the X-ray diffraction (XRD) analysis were utilized. The XRD analysis was executed using PHILIPS PW1730 XRD machine

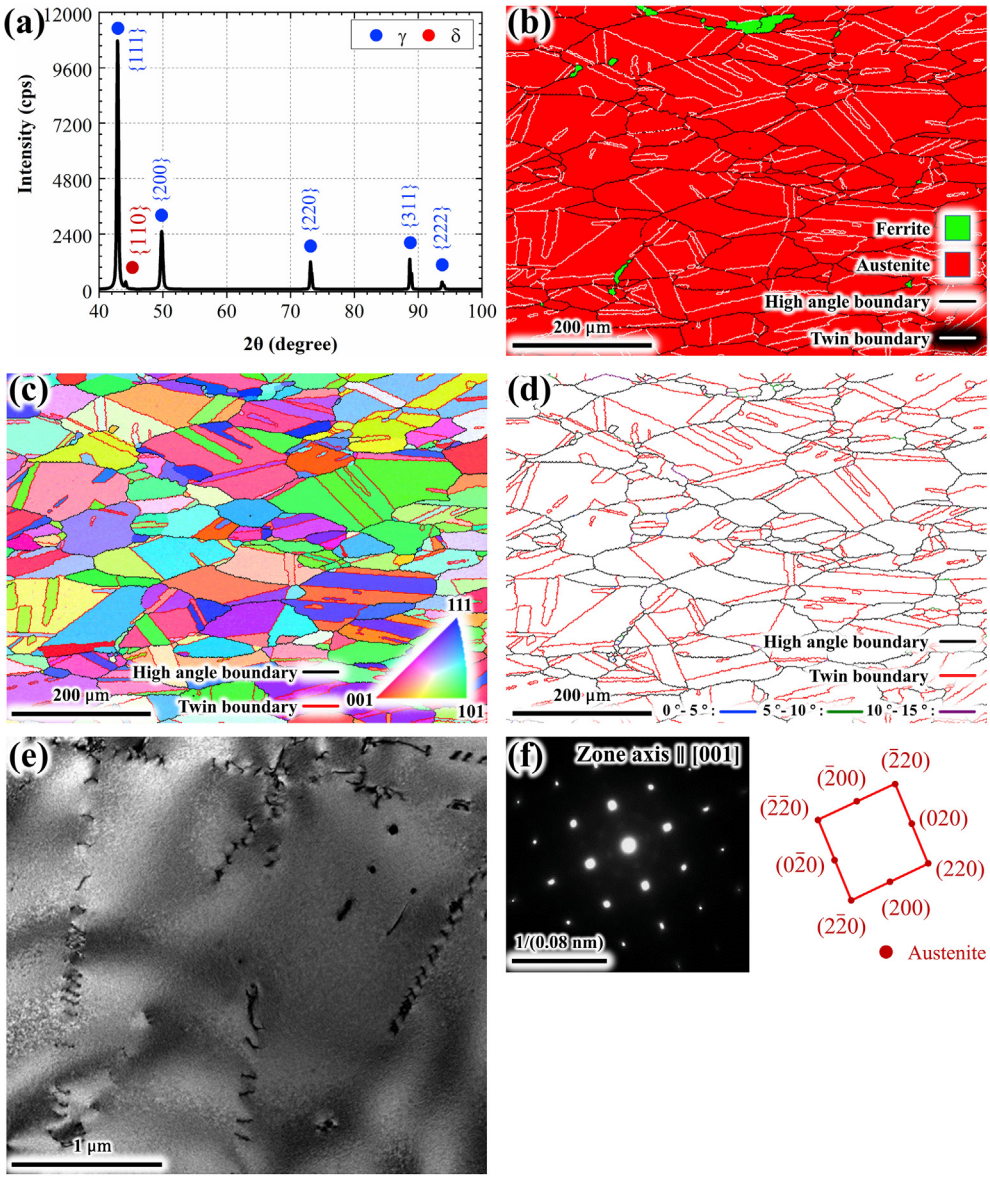

Fig. 2 – (a) The X-ray diffraction (XRD) pattern; (b) phase map; (c) inverse pole figure (IPF) map; and (d) boundary map of initial microstructure which demonstrates the presence of ~3% ferrite phase within the equiaxed austenite matrix with the average grain size of ~20 μm and ~57 μm with and without considering the contribution of annealing twins, respectively; (e) TEM micrograph of initial microstructure; (f) corresponding selected area diffraction (SAD) pattern, showing the low dislocation density with planer nature of slip in the austenite phase.

equipped with Cu-Kα radiation ($\lambda_{K\alpha}$ = 1.54056 Å) in the angle range of 10°–100° with a speed of 2.4°/min.

3. Results and discussion

3.1. *Initial microstructure*

The XRD results concerning the solution-treated material are exhibited in Fig. 2(a), which clearly represent that the major part of the microstructure is occupied by the austenite phase. Precise examination of the XRD results demonstrates that there is about 2.43% ferrite phase alongside the austenite matrix which can also be confirmed by the corresponding phase map of the initial microstructure (Fig. 2(b)) and the results of Ferritescope measurements. The negligible volume fraction of the ferrite phase beside continuity of the austenite matrix leads to the increment in strain accommodation through the austenite phase [1]. The inverse pole figure map (IPF) of the initial microstructure and the corresponding boundary map have been illustrated in Fig. 2(c) and (d), respectively. As it can be realized, the randomly texturized austenite matrix has an average grain size of 57 μm without considering twin boundaries. However, a significant number of annealing twins can be detected within the austenite phase which they have divided the austenite grains into a

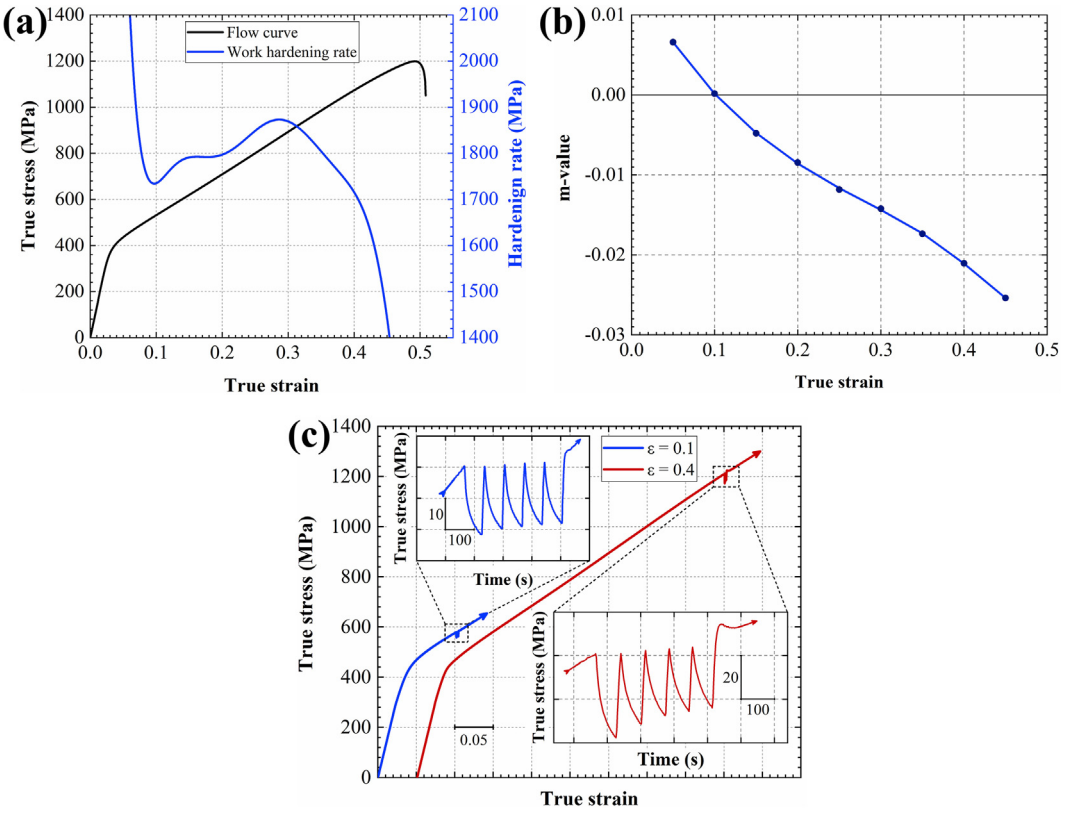

Fig. 3 – (a) The true stress–strain curve of the tensile deformation and corresponding work hardening rate at the room temperature and strain rate of 10^{-4} s^{-1}; (b) the strain rate sensitivity coefficient (m-value) curve as a function of the true strain, showing a sharp decline during monotonic loading; (c) the results of the cyclic stress relaxation test and the corresponding stress decay–time curves with the holding time of 60s at the strains of 0.1 and 0.4 which represent the apparent activation volume of 71 b^3 and 32 b^3, respectively.

lower size of 20 μm. In addition, presence of a very small fraction of low angle boundaries implies on very low energy level of the solution-treated microstructure. The TEM micrograph of the initial microstructure and its corresponding selected area diffraction pattern (SAD) are illustrated in Fig. 2(e) and (f), respectively. As is expected, the initial austenite phase displays a low density of dislocations without existence of any SF which can be attributed to the high SFE of the material.

3.2. *Room-temperature monotonic deformation behavior*

The flow stress and the corresponding work hardening rate of the experimental material are plotted as a function of true strain in Fig. 3(a). As is obvious, a significant increment in the work hardening rate can be observed. In order to examine the strain rate dependency of the material, the tensile tests were executed with different strain rates to evaluate the SRS by m-value calculation at the constant strain through the following equation:

$$m = \frac{\Delta log(\sigma)}{\Delta log(\dot{\varepsilon})} \quad (1)$$

where σ is true stress and $\dot{\varepsilon}$ is strain rate [36]. The calculated m-value has been depicted as a function of true strain in Fig. 3(b). At the beginning of plastic deformation, the SRS has a positive value that is followed by a gradual decline to negative values. It should be noted that at the strain of 0.1 the m-value reaches zero and this strain can be the onset point of strain aging during monotonic loading. It means that the dynamic strain aging (DSA) phenomenon does not take place at the beginning of monotonic loading and it may be gradually activated by proceeding the deformation. It has been demonstrated by Abedi et al. [37,38] that considering the outstanding potential of this Fe–Mn–Al–C steel for substructure development, the increment in dislocation density leads to providing high track diffusion paths through well-developed sub-boundaries which in turn can assist the carbon atoms to diffuse and subsequently pin the dislocations, thereby the probability of strain aging is enhanced. As is obvious in Fig. 3(a) and (b), the increase in the hardening rate at the strain of 0.1 coincides with the change in SRS to zero and then negative values which can indicate that the strain aging has a considerable contribution in the work hardening of monotonic deformation.

The stress relaxation test has been employed for more detailed evaluation of the governed deformation mechanism as well as to confirm the above-mentioned prediction concerning strain aging occurrence (Fig. 3(c)). In this regard, the apparent activation volume (V_{app}) and time constant (C_r) have been calculated by fitting the following equation on the stress decay results of each relaxation cycle:

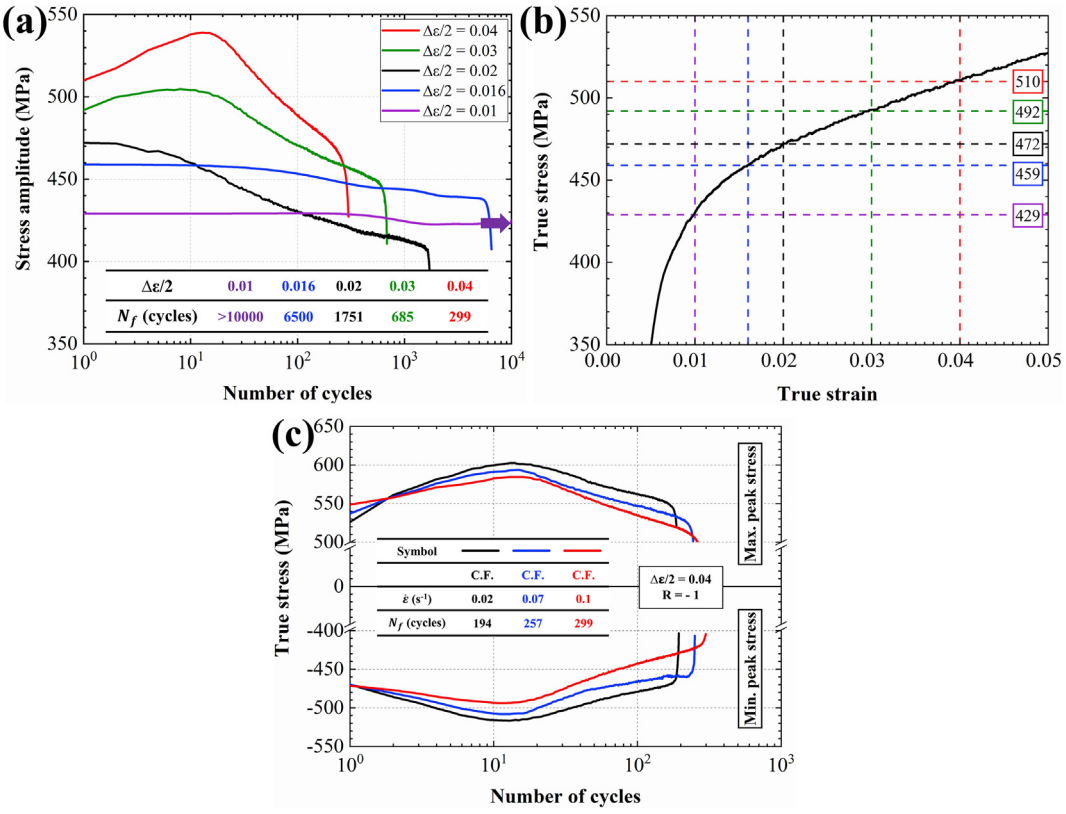

Fig. 4 – (a) The cyclic stress response curves of the conventional push–pull fatigue tests with the strain rate of 0.1 s^{-1} at different strain amplitudes (the specimen loaded at strain amplitude of 0.01 was not failed); (b) the stress levels of the material during monotonic loading at the corresponding strain levels in the course of cyclic loading; (c) the cyclic stress response curves of the conventional push–pull fatigue tests at the strain amplitude of 0.04 with the different strain rates.

$$\Delta\sigma = -\frac{M.K_B.T}{V_{app}}\ln\left(1+\frac{t}{C_r}\right) \quad (2)$$

where M, K_B, T and t are Taylor factor (M = 3.06), Boltzmann's constant (K_B = 1.3807 × 10^{-23} J K^{-1}), temperature and time, respectively [39]. The calculated V_{app} for the interrupted strains of 0.1 and 0.4 are about 71 b^3 and 32 b^3, respectively, where b^3 is Burger's vector cube (b = 0.258 nm obtained through TEM analysis). Several valuable attempts have been performed on study the deformation-induced thermally activated processes using the stress relaxation technique, in which the activation volume ranges of 0–1 b^3, 10–100 b^3, and 100–1000 b^3 are attributed to the grain boundary sliding, dislocation-point defects interactions, and forest dislocations interactions, respectively [39–41]. Accordingly, the calculated apparent activation volume of the interrupted stain of 0.1 is located at a range that belonged to the dislocation-interstitial atoms interaction as the well-known micro-mechanism of DSA. It is noteworthy that by increase in strain the V_{app} decreases that implies on increasing the probability of pinning the mobile dislocations through dislocation-interstitial interactions, consequently, more intensification in DSA manifestation which is completely in agreement with the obtained results from m-value analysis. This assertion can be rationalized through the fact that the lower apparent activation volume is stemming from the lower involved volume of the material [22].

3.3. *Room-temperature cyclic deformation behavior*

The cyclic stress response curves of the different strain amplitudes at the strain rate of 0.1 s^{-1} have been plotted as a function of the number of cycles in Fig. 4(a). As is realized, at the strain amplitudes of 0.03 and 0.04, cyclic loading behavior is characterized by cyclic hardening followed by cyclic softening to final fracture. Moreover, decreasing the applied strain amplitude effectively reduces the rate of initial cyclic hardening which leads to the appearance of pseudo-plateau behavior at the lower strain amplitudes (0.016 and 0.01). As described in section 3.2, the main reason concerning work hardening of the material during monotonic loading is room-temperature strain aging. Besides, it has been frequently observed that DSA has been recognized as the main cause of cyclic hardening and lower fatigue lives [42–45]. Accordingly, to investigate the contingency of occurrence of strain aging, the fatigue test with highest strain amplitude (0.04) has been repeated using different strain rates. Fig. 4(b) displays the

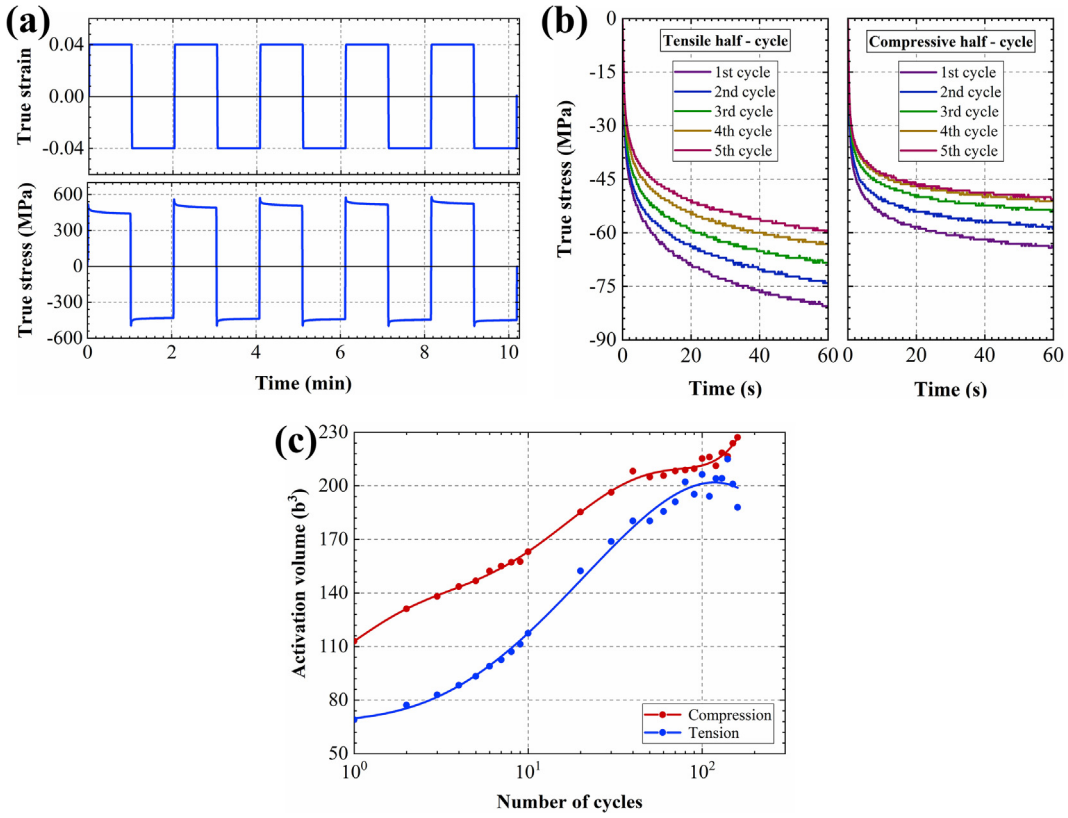

Fig. 5 – (a) The applied strain and the corresponding stress of the first five cycles of dwell-fatigue test; (b) the stress decay as a function of time for the first five tensile and compressive half-cycles; (c) the calculated apparent activation volume obtained from the stress relaxation test of each applied dwell time in the tensile and compressive half-cycles.

corresponding cyclic stress response curves for tensile and compressive half-cycles concerning applied cyclic deformation at strain amplitude of 0.04 and the strain rates of 0.02, 0.07, and 0.1 s^{-1}. As is obvious, at the first tensile half cycle, the stress level has been increased by rising the strain rate (positive strain rate sensitivity). With progressing fatigue loading, the observed positive SRS gradually turns into negative SRS behavior. It is also observed that the decrease in the applied strain rate leads to the acceleration in the cyclic hardening as well as ~35% reduction in fatigue life which can imply on the occurrence of strain aging at room-temperature cyclic deformation. The true stress–strain hysteresis loops of the cyclic deformation at the strain amplitude of 0.04 and the strain rate of 0.1 and 0.02 s^{-1} have been plotted in Fig. 4(c) and (d), respectively. As is obvious, despite negative SRS observation which is turn can be considered as one of the main evidences for DSA manifestation, neither cyclic deformation with the strain rate of 0.1 nor 0.02 s^{-1} demonstrates serrated flow behavior. It has been demonstrated by the other authors that observation of the serration in hysteresis loops cannot be considered as convincing proof to verify strain aging through room-temperature cyclic loading [44,46,47]. Additionally, variation in the fatigue life does not have the chance to be a solid reason for the occurrence of DSA [15,48]. Therefore, pieces of compelling evidence seem crucial to be obtained through more detailed analyses.

3.3.1. *Recognition of fatigue behavior through a novel method based on stress relaxation*

The stress relaxation technique is well-known as a facile and reliable method to recognize the underlying monotonic deformation micro-mechanism [49]. However, for the first time, this method was employed in our previous study in the course of dwell-fatigue loading to make better insight into dislocation response to cyclic deformation [22]. In the present study, we have tried to utilize our newly proposed method in such a way that by adding a 60s dwell time to each maximum tensile and minimum compressive half-cycles and by using the stress relaxation concept during the applied dwell time, make the governed cyclic deformation micro-mechanism reachable [22]. The responding strain and corresponding stress for the first five cycles of dwell-fatigue test are plotted as a function of the time in Fig. 5(a). As is apparent, the applied strain keeps constant during the dwell periods but the corresponding stress gradually decays which are attributed to the accommodation of the elastic strain via thermally activated dislocation glide [41,49]. To well trace the room-temperature cyclic deformation micro-mechanism, the apparent activation volume (V_{app}) has been calculated for each applied dwell period at tensile and compressive half-cycles via fitting Eq. (2) on the plotted stress decay versus time curve (Fig. 5(b)), and then plotted as a function of the number of cycles in Fig. 5(c). The V_{app} for the tensile half-cycles starts from 69 b^3, increases

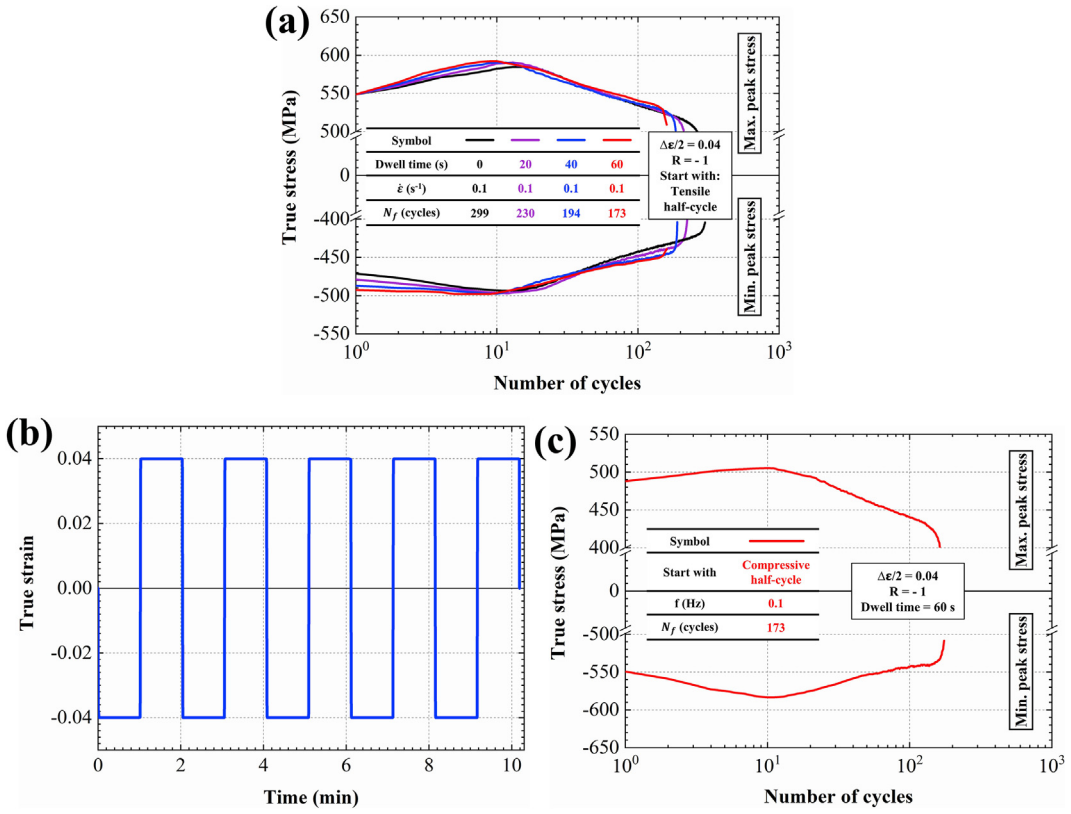

Fig. 6 – (a) The cyclic stress response curves of peak tensile and compressive half-cycles of push–pull dwell fatigue tests at the strain amplitude of 0.04 and strain rate of 0.1 s^{-1} with different dwell times (All tests started with tensile half-cycle). (b) The applied strain of the first five cycles and (c) cyclic stress response curves of peak tensile and compressive half-cycles of the repeated dwell fatigue test starting the cyclic deformation with compressive half-cycle and dwell time of 60s.

to ~100 b^3 at the 6th cycle, and then keeps the upward trend until the final fracture. But, in the case of compression, with a similar trend, the onset value of V_{app} (~110 b^3) is significantly higher than tensile mode. As mentioned before, locating the V_{app} in the range of 10–100 b^3 can be representative of dislocations–interstitials interactions. This means that the strain aging occurs at the first 6 tensile half-cycles of the room-temperature dwell-fatigue loading. Also, it can be expressed that the interaction of forest dislocations leads the V_{app} *to exceed* ~100 b^3 [39], which demonstrates that unlike tensile half-cycles, the occurrence of strain aging has been suppressed at the compressive half-cycles. This clearly denotes the difference between deformation micro-mechanisms of the tensile and compressive half-cycles of the dwell-fatigue.

In order to verify the effect of applying dwell time on the cyclic behavior of material, the dwell fatigue test has been repeated with dwell times of 20 and 40s. The cyclic stress response curves of peak tensile and compressive half-cycles of dwell fatigue tests with dwell times of 20, 40 and 60 s alongside conventional fatigue have been plotted in Fig. 6(a). Obviously, the conventional fatigue (dwell time of 0s) manifests a slight asymmetrical behavior in the course of tensile and compressive half-cycles. However, applying the dwell time leads to the intensification of this asymmetrical behavior, so that increasing in the applied dwell time makes the rate of cyclic hardening substantially increase for tensile half-cycles and decrease for compressive half-cycles. In addition, the absolute stress value of the first compressive half-cycle concerning the dwell-fatigue is remarkably higher than the conventional fatigue. Additionally, in order to confirm the influence of dwell time on the intensification of stress asymmetry, the dwell fatigue test with the strain amplitude of 0.04, strain rate of 0.1s^{-1}, and dwell time of 60s has been repeated by applying the first half cycle in compression mode instead of tension (the imposed strain as a function of time has been plotted in Fig. 6(b)). The corresponding cyclic stress response curves for peak tensile and compressive half-cycles have been plotted in Fig. 6(c). It is clear from the results that the material cyclically hardens during first 10 compressive half-cycles while in the case of tensile half-cycles, it exhibits lower rate of cyclic hardening. Accordingly, intensification of the asymmetrical behavior during dwell fatigue is totally related with the mode of the first applied half cycle.

The peak tensile and compressive stresses for the dwell-fatigue (with applying the first half cycle in tension mode) is compared with the corresponding curves for the conventional fatigue at the different strain rates in Fig. 7(a). It was clearly demonstrated that decreasing the strain rate accompanying

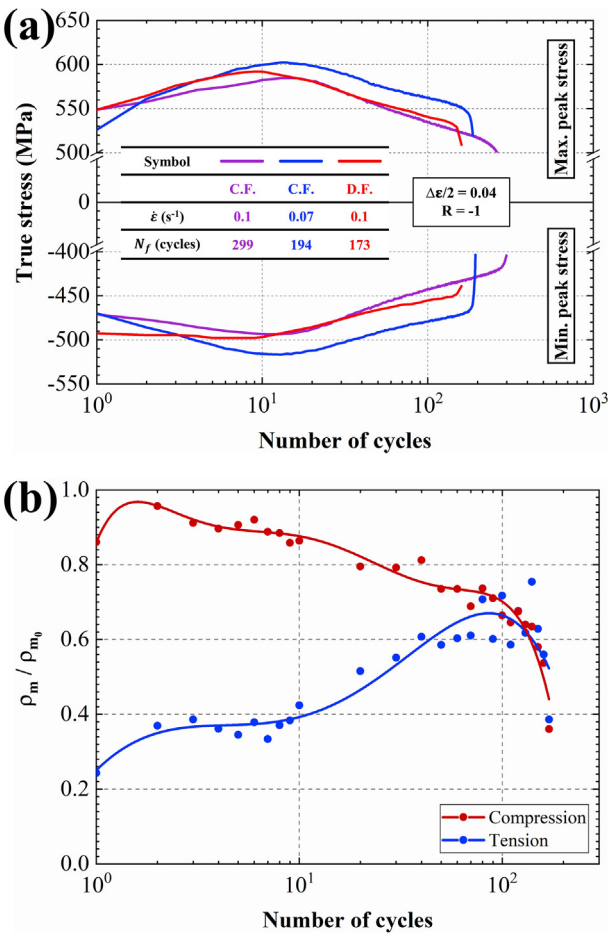

Fig. 7 – (a) Comparison between peak tensile and compressive stresses as a function of the number of cycles for dwell-fatigue (D.F) and conventional fatigue (C.F) with the different strain rates; (b) evolution of the mobile dislocation density (ρ_m / ρ_{m_0}) after the relaxation of each tensile and compressive stresses during the dwell-fatigue loading.

with applying dwell time make the rate of cyclic hardening to increase. It is worth noting that the DSA phenomenon can effectively make the dislocation glide difficult which in turn leads to a considerable work hardening rate of monotonic and cyclic deformations. Hence, an increment in the cyclic hardening rate during conventional fatigue with a decrement in the strain rate would be a result of the occurrence and/or acceleration of strain aging phenomenon. Similarly, the cyclic hardening rate of peak tensile stress in dwell-fatigue is completely in agreement with the obtained results of activation volume which demonstrate that the DSA is the dominant deformation micro-mechanism in primary tensile half-cycles. On the contrary, pseudo-plateau behavior of peak compressive stress can be stemming from the suppression of DSA phenomenon.

In order to well trace the dislocation response to the dwell time and also decipher the asymmetrical behavior of the dwell-fatigue, the calculation of mobile dislocation density (ρ_m / ρ_{m_0}) is considered. For this purpose, based on the empirical relationship between (ρ_m / ρ_{m_0}) and dislocation velocity (v) [39,49], and the proposed correlation between dislocation density and dislocation velocity by Orowan [50], it can be shown that [49]:

$$\left(\frac{\rho_m}{\rho_{m_0}}\right) = \left(\frac{C_r}{t + C_r}\right)^{\left(\frac{\beta}{1+\beta}\right)} \quad (3)$$

where ρ_m is the density of mobile dislocations at the moment of t, ρ_{m_0} is the density of mobile dislocations at the first moment of stress relaxation (t = 0), and β is the dimensionless immobilization parameter [39,49]. The related calculations concerning effective parameters have been precisely and comprehensively expressed in our previous study [22]. The calculated (ρ_m / ρ_{m_0}) is plotted versus the number of cycles in Fig. 7(b). As is realized, in the first 10 cycles, there is a notable difference between the mobile dislocation density of tensile and compressive half-cycles. The (ρ_m / ρ_{m_0}) value concerning tensile mode is started from the 0.24 and increases to higher values of ~0.7, while in the course of compressive mode, it is reduced from 0.86 to ~ 0.7. Since (ρ_m / ρ_{m_0}) represents the ratio of density of mobile dislocations at the end of dwell period to initial density of mobile dislocations, the reduction in (ρ_m / ρ_{m_0}) value can be attributed to more dislocation immobilization during the dwell period. In this respect, unlike compressive half-cycles, a noticeable fraction of mobile dislocations has been immobilized during tensile half-cycles. As a result, the simultaneous occurrence of dislocation immobilization and cyclic hardening at the primary tensile half-cycles indicates that the interstitial atoms pin the moving dislocations. The consequence of this work hardening can also be observed at the following compressive half-cycle which results in a higher stress level in compressive half cycles in respect to tensile mode during the dwell-fatigue loading.

3.4. *Fatigue damage*

The fracture surface, as an exhibitor of the main and secondary cracks, has the required potential to unveil the fatigue properties of the material and also be a representative the footprints of the microstructural evolutions, therefore, plays an eminent role in understanding the cyclic deformation behavior [21,51–59]. Since the fatigue damages and failures are stemming from the strain localization, and considering that the DSA has been diagnosed as the main phenomenon during cyclic loading in the current study, the fracture behavior investigations seem necessary. For this purpose, macroscopic overview of the fracture surface of conventional fatigue samples with different strain rates as well as the dwell-fatigue sample (at the strain amplitude of 0.04) is examined and illustrated in Fig. 8. The crack initiation sites and the final fracture zone of each condition have been marked by red arrow and yellow dashed line, respectively. As is obvious, the conventional fatigue with high strain rate has experienced a multiple crack initiation with 7 initiation sites which its number effectively is reduced by decreasing the strain rate, and changes into single initiation site in dwell-fatigue sample. Also, it is clearly recognizable that the final fracture region has been expanded by decreasing the strain rate and applying dwell time.

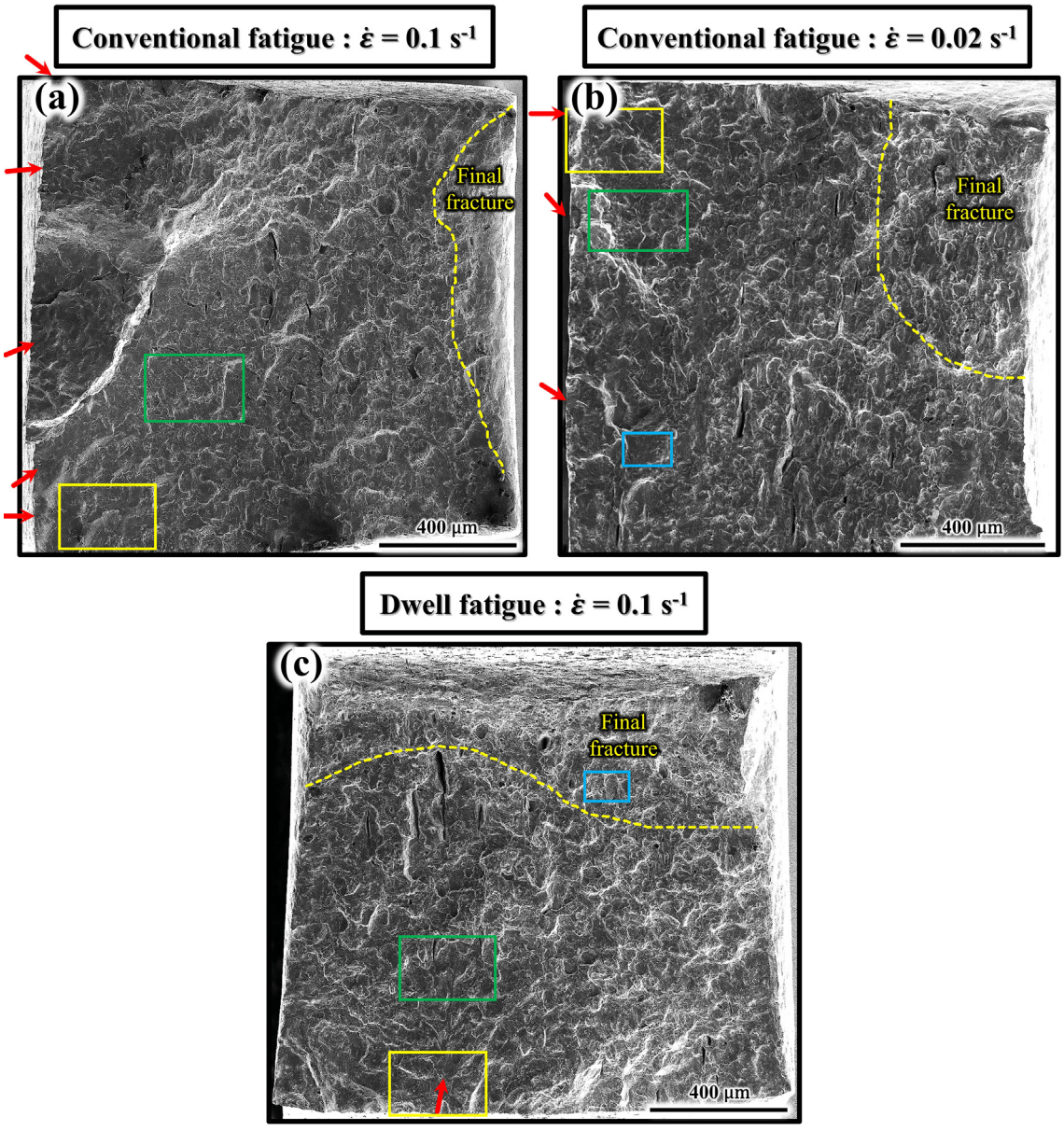

Fig. 8 – The macroscopic fracture surface of cyclically loaded specimens at strain amplitude of 0.04: (a) conventional fatigue with high strain rate; (b) conventional fatigue with low strain rate; (c) dwell-fatigue, showing the decrement in the number of initiation sites and increment in the final fracture areas through decrease in strain rate and applying dwell time. The colored rectangles declare the position of high magnification SEM images which have been represented in Figs. 9 and 14.

The crack propagation region for all conditions is compared at equal distances from the initiation site in Fig. 9. In this respect, the average fatigue striation spacing has been measured at the low and high stress intensity factor range (ΔK) levels and noted by yellow in corresponding. Low and high ΔK regions are attributed to the early and stable crack propagation regions which are marked via yellow (Fig. 9 (a–c)) and green (Fig. 9 (d–f)) rectangles, respectively. Each fatigue striation is attributed to a single fatigue cycle which means that the variations in striation spacing are directly related to the crack growth rate [21,60]. As can be seen, at the low ΔK level, the fatigue striations are not well-defined in the cyclically loaded sample with high strain rate (Fig. 9(a)) and they are not large enough to be confidently measured. However, these striations become well-defined by decrement in the strain rate (Fig. 9(b)). In addition, it can be clearly observed that the striation spacing significantly increases by applying the dwell time (Fig. 9(c)). By comparison between the fatigue striation spacings of these samples at the high ΔK level, it can be seen that it is approximately identical for all samples (Fig. 9(d–f)). It can be concluded that the crack growth rate increases by decreasing the strain rate as well as applying the dwell time. The deformation localization through DSA effectively restricts the plastic deformation at the fatigue crack tip, thereby increasing the crack growth rate [42,45,61]. Increasing the final fracture area is another effect of plastic deformation restriction which increases by decreasing the strain rate and applying the dwell time.

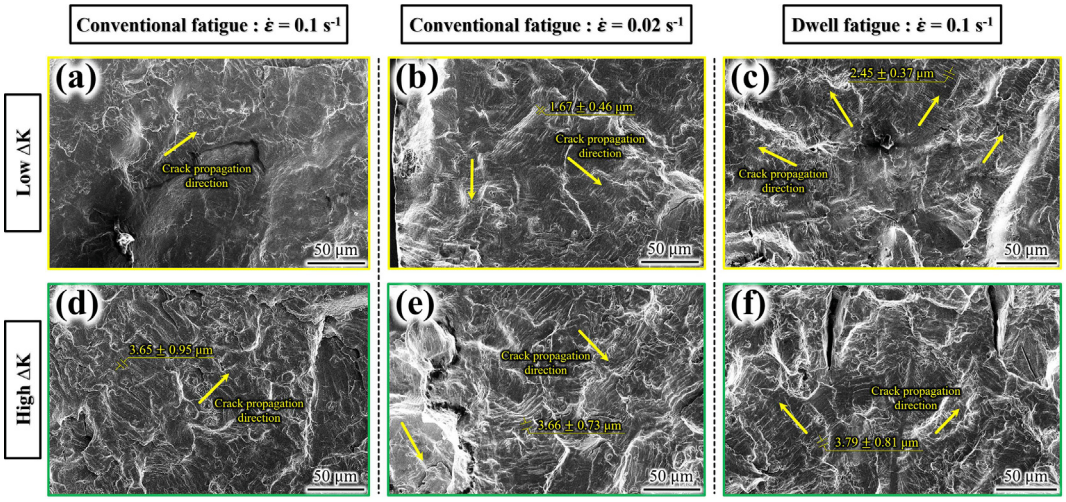

Fig. 9 – High magnification FE-SEM fractographs from the crack propagation region of cyclically deformed samples under (a,d) conventional fatigue with high strain rate, (b, e) conventional fatigue with low strain amplitude and (c, f) dwell fatigue; (a–c) close to initiation site (low ΔK); (d–f) far from initiation site (high ΔK). The positions of the magnified images of low and high ΔK regions are signed in Fig. 8 using the yellow and green rectangles respectively.

3.4.1. *Microstructural origin*

To study the microstructural aspects of the cyclically deformed material with the aim of confirming the above-mentioned assertions and also developing the involved micro-mechanism concerning the room-temperature strain aging during cyclic deformation, the evolution of dislocation structures has been fully observed. For this purpose, STEM micrographs of the cyclically deformed sample at the strain amplitude of 0.04 and strain rate of 0.02 s^{-1} as well as the corresponding SAD pattern are illustrated in Fig. 10(a) and (b), respectively. The indexed SAD pattern clearly demonstrates that the STEM micrograph has been provided within the austenite grain at the zone axis of [−110]. As is obvious, two distinct regions ((c) and (d) regions) with different dislocation configurations can be distinguished through an annealing twin boundary. The higher magnification of the signified regions in Fig. 10(c) and (d) clearly reveals the character of slip is mostly planar and also related planar slip traces can be diagnosed which are marked by colored lines and noted by A, B, and C. The dislocations with the planar character are more obvious in region (d) compared to region (c) which can be due to different Schmid factors of these regions. Recently, a number of researches have demonstrated that the slip character of dislocations can alter from planar to wavy through cyclic deformation even in low SFE materials [21,62,63]. In contrast, it has been proved that the DSA restricts the cross slip which in turn promotes the strain localization, thereby inducing the long-range planarity of dislocation in the microstructure [42,44,64]. In the present work, considering the high potential of the studied material to incur the extensive substructure development during straining [37], it is expected that the wavy slip character should be observed. But, cyclic deformation-induced reversible dislocation movement leads to the long-range planarity through expediting the strain aging and therefore observation of planar slip traces during cyclic deformation.

It is worth mentioning that the single SFs can be detectable in Fig. 10(c) which are signified by yellow arrows. Interestingly, wide SF regions are also visible at the interaction of A and B slip traces which are shown via light green arrows in Fig. 10(d). In this connection, Fig. 11(a) schematically displays the pinning of a mobile partial dislocation by the interstitial atoms. A full dislocation (a/2<110>) dissociates to leading and trailing partial dislocations (a/6<112>) bounding a stacking fault (which is narrow in the high SFE materials). The carbon atoms can diffuse to the dislocation core and reduce the moving ability of the partial dislocations. Opening up a fast diffusion channel near the core of trailing partial facilitates its pining by the interstitials, but absence of this channel near the leading partial leads to different mobility of leading and trailing partials and therefore widening of the SF region [65]. Accordingly, the existence of dislocations with wide SF regions (shown by light green arrows in Fig. 11(b) and (c)) beside the dislocations with narrow SF regions (signified by yellow arrows in Fig. 11(b) and (c)) are observable which can be due to the strain aging phenomenon. It should be pointed out that dislocations with narrow SF regions may be also developed by subsequent closure of SF regions through reversible movement of Shockley partial dislocations. Also, some of the partial dislocations remain unpinned during cyclic deformation, thereby widening the SF regions does not occur.

3.4.2. *Mechanism of room-temperature DSA during conventional and dwell-fatigue*

As is comprehensively discussed earlier, strain aging is the dominant phenomenon during the primary cycles of the

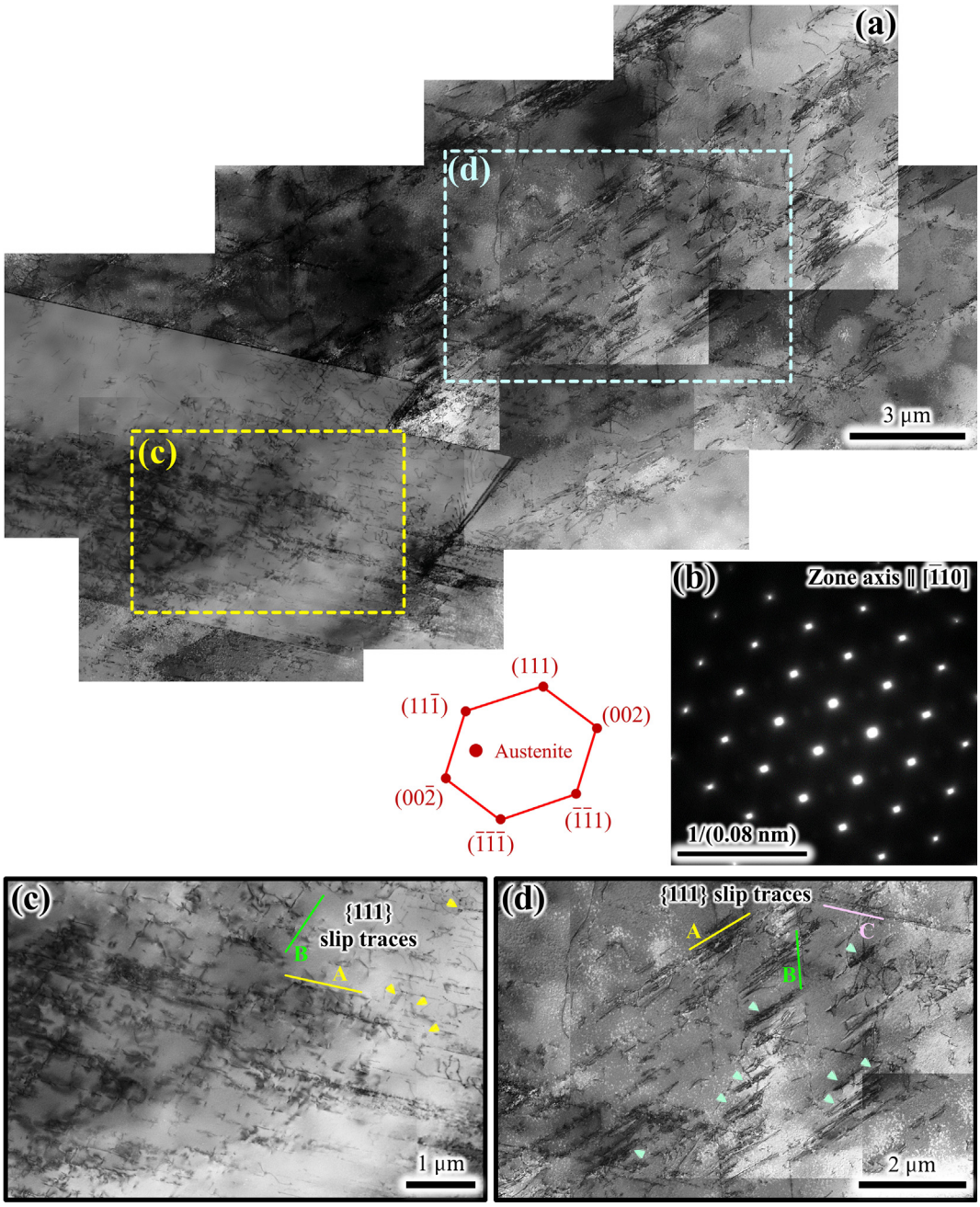

Fig. 10 – (a) The scanning transmission electron microscopy (STEM) bright-field micrograph related to the microstructure after fully reversal conventional fatigue loading at the strain amplitude of 0.04 and strain rate of 0.02 s^{-1}; (b) the corresponding SAD pattern that illustrates the single austenite phase (zone axis for austenite phase is [−110]); (c) and (d) higher magnifications of the STEM image that clearly represent the planar glide of dislocations, single wide stacking fault (SF) regions (pointed by yellow arrows), and wide SF regions located at the intersections of A and B slip traces (pointed by light green arrows).

room-temperature cyclic deformation in the studied material. The corresponding micro-mechanism should be developed and specified for the cyclic deformation. In this regard, Fig. 12 has been schematically drawn to clarify the proposed micro-mechanism and the main steps of that are described below:

(I) At the initial stage, randomly distributed dislocations exist in the different slip systems.

(II) At the first tensile half-cycle, a limited number of dislocations interact with the carbon atoms. Pinning the trailing partials by interstitials would lead to the different moving abilities of the partial dislocations which directly increases the width of the SFs.

(III) Unloading the tensile stress and then applying the compressive stress would make the dislocations to glide in the reverse direction on the same slip system.

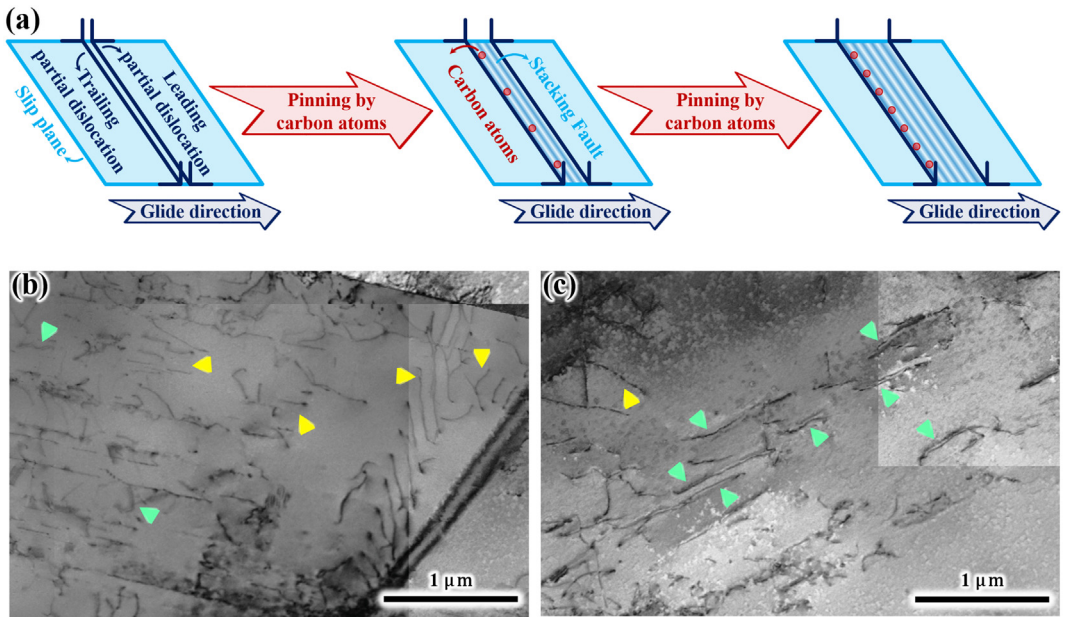

Fig. 11 – (a) The schematic view of pinning the trailing partial dislocation by carbon atoms which leads to widening the SF region. Close-up STEM image showing the (b) dislocations with narrow (pointed by yellow arrows) and (c) wide (pointed by light green arrows) SF regions.

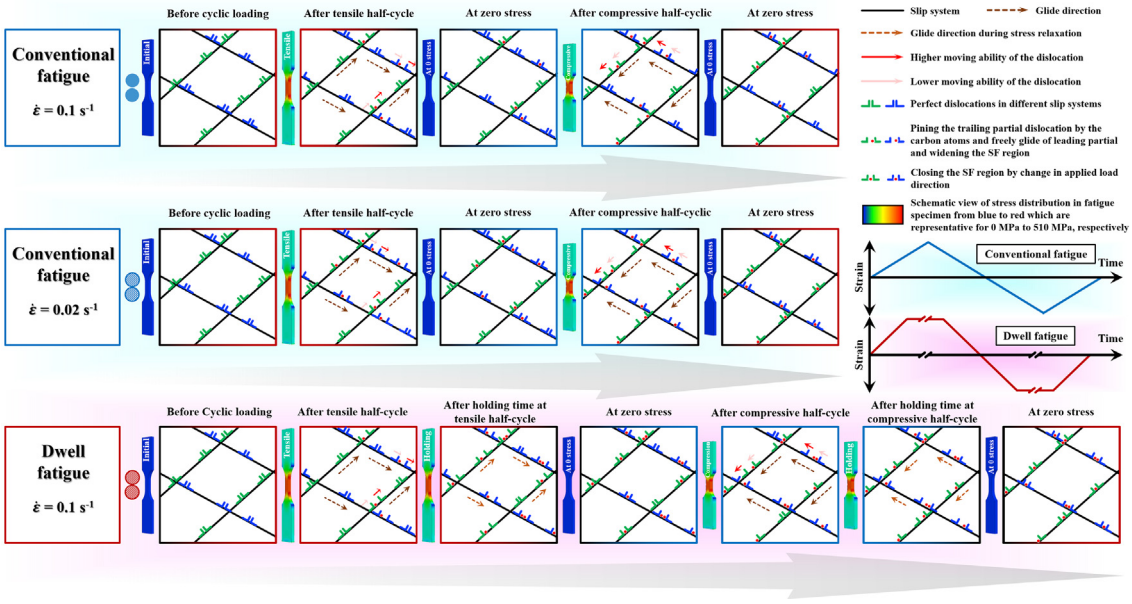

Fig. 12 – The schematic view of the dislocation-carbon atom interaction during the cyclic deformation based on reversible dislocation movement. The detailed micro-mechanism of dynamic strain aging (DSA) occurrence during conventional fatigue (C.F) with different strain rates and dwell-fatigue (D.F) has been explained. Dislocation pinning by carbon atoms randomly occurs in the course of first tensile half-cycle and continues during the compressive mode. This behavior intensifies by decreasing the strain rate. Appling the dwell time at the maximum tensile stress strongly increases the probability of trailing partials pinning through carbon atoms. This significantly reduces the un-pinned SF regions which in turn can diminish the possibility of the dislocation pinning during compressive half-cycle.

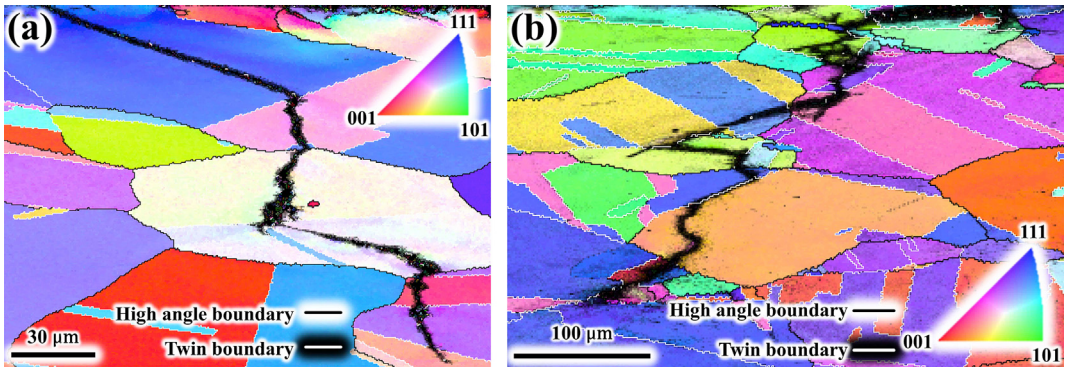

Fig. 13 – The IPF map of the secondary crack in the cross-sectional view of the cyclically deformed samples at the strain amplitude of 0.04 and strain amplitudes of (a) 0.1 and (b) 0.02 s^{-1}.

Consequently, most of the opened SFs would be closed at the zero stress level.

(IV) Reversible dislocation movement would significantly increase the probability of dislocation-carbon atoms and dislocation–dislocation interactions. This would effectively reduce the dislocation velocity and intensify DSA occurrence.

(V) Unloading the compressive stress would again make the SFs to be closed which leads most of the visible dislocations to have narrow SF region in the microstructure.

(VI) During dwell-fatigue, holding the strain during the dwell period would provide the required time for diffusion of carbon atoms to extensively pin the existing dislocations.

(VII) Applying the dwell time at the compressive half-cycle would cause the dislocations to be pinned not as much as tensile half-cycle, since during tensile dwell time, most of the available dislocations have been pinned which in turn reduces the probability of dislocation pinning at the next half-cycle.

Evidently, the above described micro-mechanism steps are convincingly in compliance with the evolution of mobile dislocation density as well as cyclic stress responses. It should be emphasized that the reduction in strain rate provides the needed time for the above-mentioned interactions which results in more dislocation pinning (Fig. 11). Moreover, with detailed observation of Fig. 7(a), during conventional fatigue, the stress level of the first tensile half-cycle at the higher strain rate condition is considerably greater than lower strain rate (positive SRS), while the compressive stress level is the same for both conditions. Thus, it can be derived that the DSA may not effectively manifest during the first tensile half-cycle and there is no difference between the first half-cycle and monotonic loading. However, the reversible movement of dislocation accelerates the occurrence of strain aging during the next half-cycles, causing to observe negative SRS.

As declared in steps (VI) and (VII) of the proposed micro-mechanism, a significant potential for the DSA is consumed during the first holding time at the maximum tensile stress. Also, the subsequent compression cannot effectively enhance the population of unpinned dislocations (through the unpinning of the pinned dislocations and/or dislocation generation). These significantly harden the dislocation glide and consequently, the higher stress level is obtained for the subsequent compressive half-cycle (Fig. 7(a)). In addition, the lower

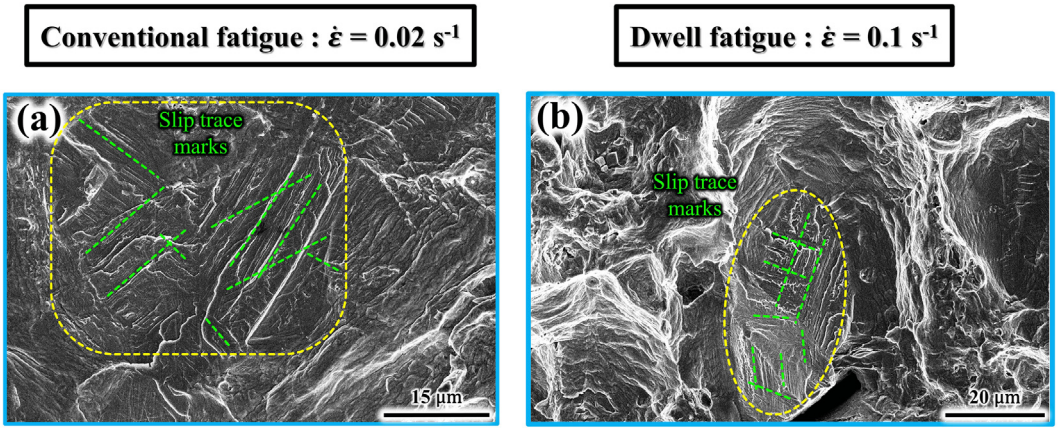

Fig. 14 – The footprints of long-range planar slip within the (a) crack propagation and (b) final fracture regions of cyclically deformed samples under conventional fatigue with lower strain rate and dwell fatigue, respectively. They show the significant role of the planarity of slip even at over-load stage. The position of each magnified image is signed by the blue rectangle in Fig. 8.

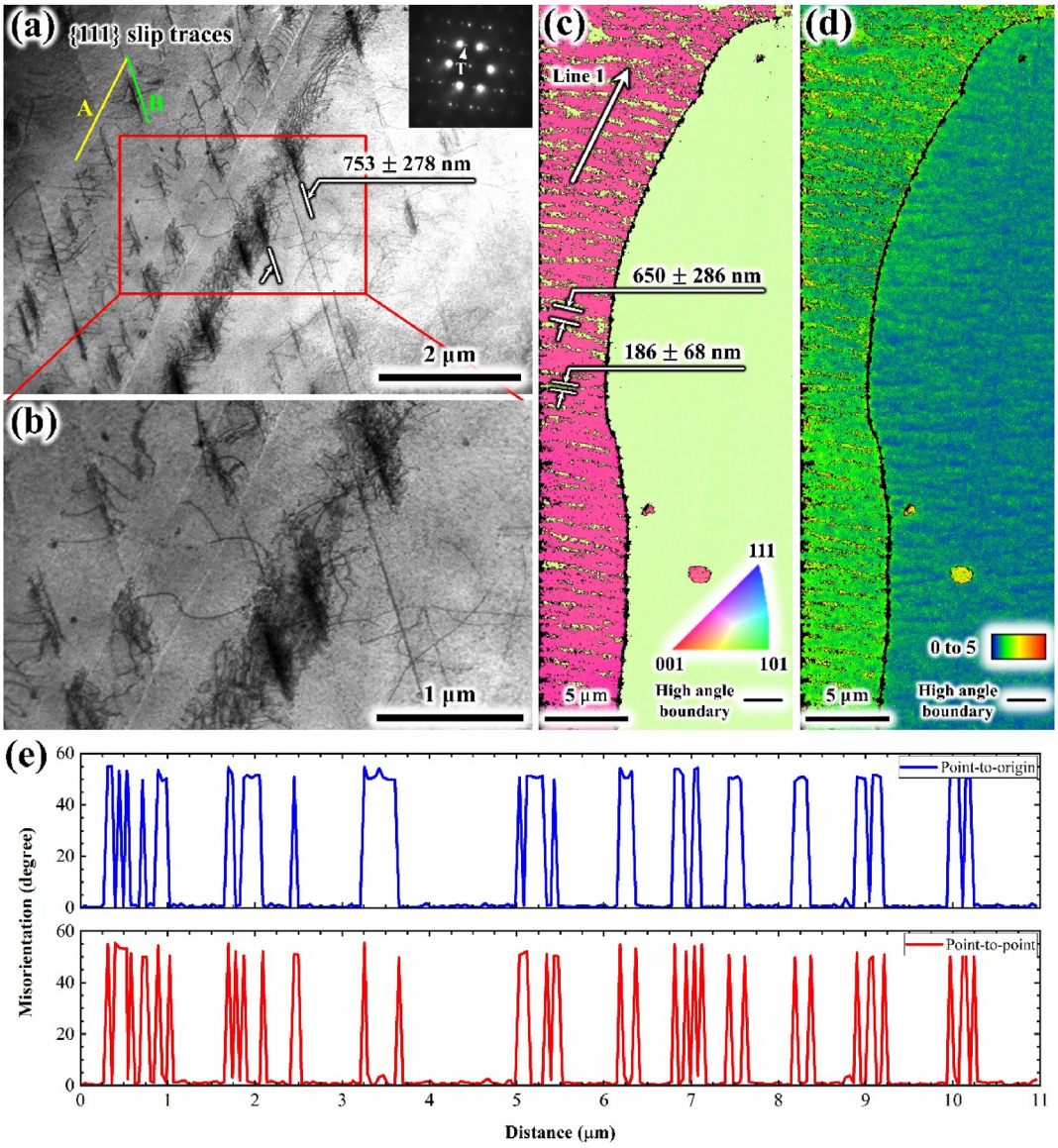

Fig. 15 – (a) TEM micrograph and (b) its magnified view (from the zone axis of [−110]) corresponding to the cyclically deformed microstructure at the strain amplitude of 0.04 and strain rate of 0.02 s^{-1} illustrate twinning at the intersection of A and B slip traces. High-resolution electron back-scatter diffraction (HR-EBSD) analysis of the same microstructure; (c) the IPF and (d) KAM maps demonstrate parallel deformation bands at the vicinity of the grain boundary; (e) the misorientation profiles along line 1 verify the twin nature of these bands. The thickness and the intervals of twin bands in the HR-EBSD results and TEM micrograph are also noted.

fraction of unpinned dislocations would suppress the occurrence of DSA at the compressive half-cycles.

3.4.3. *Damage mechanism*

In order unveil the overlooked influence of dynamic strain aging on the fatigue crack behavior the crack path has been characterized by performing the EBSD analysis on the secondary crack path of the cyclically deformed samples at the strain rates of 0.1and 0.02 s^{-1} and the corresponding IPF maps have been illustrated in Fig. 13(a) and (b), respectively. As is obvious from the results, the cyclically deformed material under the strain rate of 0.1s^{-1} showed transgranular crack propagation whereas decreasing in strain rate converted the crack propagation mode from transgranular to intergranular. It has been demonstrated by Zhou et al. [66] that occurrence of the strain aging during cyclic deformation of an austenitic steel facilitates the formation of planar slip bands and their interaction with grain boundaries causes stress concentration at those regions which in turn intensifies the formation of intergranular micro-cracks. Moreover, it has been described before that lowering the strain rate stimulates strain aging phenomena during fatigue loading. Consequently, as the strain rate decrease, the crack propagation mode gradually transfers from transgranular to intergranular. Magnified fractographs in Fig. 14(a) and (b) represent the linear feature (specified by green dashed lines) within the crack propagation

region related to the conventional fatigue with lower strain rate and final fracture region related to the dwell-fatigue, respectively. By comparison of these features with the STEM micrograph, it can be realized that the intervals of these lines in the fracture surface are approximately identical with the intervals of the slip traces in STEM image. It means that the above-mentioned characteristic as a footprint of slip traces in the fracture surface, is stemming from the long-range planarity of slip. Considering this fact that intersection of slip traces with boundaries or other slip traces can act as stress concentration sites, manifestation of the slip trace marks in the fracture surface of lower strain rate as well as dwell fatigue demonstrate that acceleration of DSA motivate the intergranular cracking which is totally in agreement with the results of EBSD analysis from secondary crack paths. Prevailing the intergranular cracking along with restriction the plastic deformation around the crack tip can significantly accelerate the crack propagation as well as final fracture.

3.4.4. *Dynamic strain aging induced deformation twinning*

Deformation twin formation is an unexpected phenomenon in cyclic deformation of the studied material due to (i) low imposed strain during cyclic deformation and (ii) high SFE of the material. Fig. 15(a) and (b) display the magnified TEM micrographs from the wide SFs located at the intersection of A and B slip traces. The nature of the appeared feature at the slip traces' intersection is diagnosed via SAD pattern analysis (Fig. 15(a)) which indicates that the deformation twin is the essence of these wide SFs. As is previously discussed, the occurrence of DSA can cause the widening of the SF regions through the pinning of trailing partial dislocations. It has been demonstrated by Koyama et al. [67] that the occurrence of strain aging during monotonic loading reduces the required critical strain for deformation twinning through widening the SF regions as well as random stacking of extended dislocations. In the case of cyclic deformation, besides intensifying the occurrence of strain aging, reversible dislocation movement can effectively enhance the probability of overlapping of developed SFs, thereby providing the proper condition for twinning.

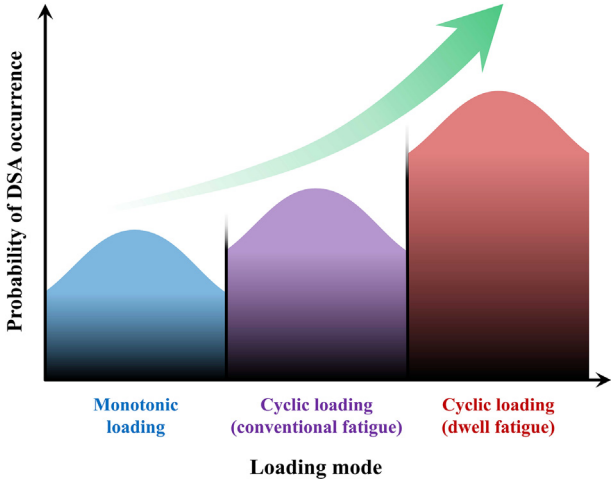

Fig. 16 – Schematic diagram demonstrating the probability of the occurrence of the strain aging against the loading mode. With the change in loading mode from monotonic to cyclic and then conventional fatigue to dwell-fatigue, the possibility of DSA manifestation will have been increased.

To prove this assertion concerning the deformation twinning as a result of DSA, the HR-EBSD analysis has been employed. In this regard, the IPF and KAM maps of the cyclically deformed microstructure under the strain amplitude of 0.04 and strain rate of $0.02s^{-1}$ are illustrated in Fig. 15(c) and (d), respectively. As is obvious, numerous deformation bands-like have been parallelly formed at the vicinity of the grain boundary of the left grain. The intervals and the thickness of these bands are almost equal with the demonstrated twin bands in TEM micrographs which emphasize that these features are representative of an identical phenomenon. Moreover, the misorientation profiles along line 1 have been plotted in Fig. 15(e). As is realized, the misorientation of these bands with the matrix is almost in accordance with the Σ3 boundaries (which is about 60° in the FCC crystal structure [40,68]) which can compellingly confirm that the nature of deformation bands-like is the deformation twin. It should be mentioned that the formation of twins would not eliminate the present slip traces, therefore, continuation of cyclic deformation leads to increasing the dislocation density around the deformation twin and in turn enhances the interaction of dislocations with twin boundaries. In addition, some of the observed bands can be related to the twin embryos, where the overlapping of SFs has not been completely performed [40]. Thus, the microstructure containing the mixture of twins and twin embryos as well as distorted twin boundaries due to subsequent deformation shows some deviated misorientation from 60° (Fig. 15(e)).

According to the exhibited results, it can be deduced that providing the proper condition for deformation twinning through strain aging and slip planarity can influence on crack initiation behavior. In such a way that the intersection of slip traces can potentially act as the crack initiation site stemming from the stress concentration. In this connection, characterizing the influence of deformation twinning on crack behavior seems noteworthy and precious. As is obvious in Fig. 15(b), the KAM value of the twin bands is very high that implies the accommodation of a significant amount of strain through deformation twinning. Frequent formation of twins all over the microstructure at the intersection of slip traces during cyclic deformation would retard the micro-voiding, thereby defer the micro-cracking which leads to reduce the number of crack initiation sites at the conventional fatigue with the strain rate of $0.02s^{-1}$ and the dwell-fatigue (Fig. 8 (b) and (c)). However, to justify the reduction in fatigue life of these conditions, this point should be considered that, at the low-cycle fatigue regime, the crack growth stage is dominant.

3.5. *Effect of loading mode on the occurrence of DSA*

Alteration in the loading mode effectively affects the dislocation movement and through it, impacts the dislocation-based phenomena. As described before, the SRS is positive at the beginning of the monotonic deformation. Formation of well-developed dislocation substructure through straining accelerates the stress-assisted diffusion of the carbon atoms [37], which means that the occurrence of strain aging phenomenon

is not probable at the low imposed strains and also it is intensified by continuing the monotonic deformation. Surprisingly, applying the cyclic deformation even with a lower imposed strain in respect to monotonic deformation, provides the reversible movement of dislocation which encourages the occurrence of strain aging. It has been well demonstrated that applying the dwell time to the conventional cyclic loading would intensify the influence of reversible dislocation movement by providing sufficient time for the diffusion of carbon atoms. In this context, Fig. 16 schematically demonstrates the remarkable increment of the probability of the strain aging occurrence by variation in the loading mode.

In the current study, the onset of DSA has received more attention, however, according to the mobile dislocation density analysis in section 3.3.1 as well as the cyclic hardening and cyclic softening behavior throughout the fatigue deformation, it can be derived that the severity of DSA manifestation is gradually disappeared in dwell-fatigue by the increase in the number of cycles. This is completely contrary to the DSA behavior in the course of monotonic deformation. This gradual disappearing of strain aging is stemming from the diminishing of the effectiveness of reversible dislocation movement due to the various reasons i.e. enhancement in dislocation density with increasing the number of cycles [22,69], persistent slip band formation [69,70], etc. inducing the irreversible dislocation movement. These findings would be the most prominent created differences by alteration in the loading mode from monotonic to cyclic.

4. Conclusion

In this paper, it was attempted to figure out fatigue properties and the response of Fe-17.5Mn-8.3Al-0.74C-0.14Si lightweight steel to room-temperature cyclic deformation through the new method based on stress relaxation during dwell-fatigue as well as the comprehensive microstructural characterization. The main findings can be summarized as follows:

1. The occurrence of the room-temperature strain aging during cyclic deformation seemed to be theoretically impossible owing to the low imposed strain and low diffusion rate. This phenomenal occurrence was justified through the fact that the cyclic deformation-induced reversible dislocation movement intensifies the interaction of dislocations with interstitial solute atoms.
2. Applying the dwell time at the peak tensile half-cycles provided the required time for pinning the majority of the mobile dislocations which led to the significant increase in the absolute stress value and also the lower potential for DSA at the next compressive half-cycles.
3. The occurrence of DSA was accompanying with pinning the trailing dislocations and widening the SF regions. As a side effect, this could restrict the cross slip and develop the long-range planarity which was identified as slip trace marks in the fracture surface.
4. Stimulating the interaction of the slip traces with the grain boundaries as well as other slip traces by providing the proper conditions for dynamic strain aging can facilitate micro-viding and micro-cracking at grain boundaries which in turn can change the mode of crack growth from transgranular into intergranular.
5. Development of wide SFs at the intersection of slip traces and subsequent overlapping of them led to deformation twinning, which in turn could result in fatigue crack initiation retardation by accommodating a significant amount of strain.
6. Change in loading mode from monotonic to cyclic deformation, and conventional fatigue to dwell-fatigue caused the acceleration in onset of room-temperature strain aging in a low-density steel.

Declaration of Competing Interest

The authors declare that they have no known competing financial interests or personal relationships that could have appeared to influence the work reported in this paper.

Acknowledgements

This work was supported by the Korea University Grant for S.S. Sohn, by Korea Institute for Advancement of Technology (KIAT) grant funded by the Korea Government (MOTIE) (P0002019, The Competency Development Program for Industry Specialist). Also, the authors acknowledge the support of the Academy of Finland for the ''Genome of Steel'' project #311934.

REFERENCES

[1] Chen S, Rana R, Haldar A, Ray RK. Current state of Fe-Mn-Al-C low density steels. Prog Mater Sci 2017;89:345–91. https://doi.org/10.1016/j.pmatsci.2017.05.002.
[2] Zuazo I, Hallstedt B, Lindahl B, Selleby M, Soler M, Etienne A, et al. Low-density steels: complex metallurgy for automotive applications. J Occup Med 2014;66:1747–58. https://doi.org/10.1007/s11837-014-1084-y.
[3] Rana R. Low-density steels. J Occup Med 2014;66:1730–3. https://doi.org/10.1007/s11837-014-1137-2.
[4] Zambrano OA. A general perspective of Fe–Mn–Al–C steels. J Mater Sci 2018;53:14003–62. https://doi.org/10.1007/s10853-018-2551-6.
[5] Yoo JD, Park K-T. Microband-induced plasticity in a high Mn–Al–C light steel. Mater Sci Eng A 2008;496:417–24. https://doi.org/10.1016/j.msea.2008.05.042.
[6] Welsch E, Ponge D, Hafez Haghighat SMM, Sandlöbes S, Choi P, Herbig M, et al. Strain hardening by dynamic slip band refinement in a high-Mn lightweight steel. Acta Mater 2016;116:188–99. https://doi.org/10.1016/j.actamat.2016.06.037.
[7] Frommeyer G, Brüx U. Microstructures and mechanical properties of high-strength Fe-Mn-Al-C light-weight TRIPLEX steels. Steel Res Int 2006;77:627–33. https://doi.org/10.1002/srin.200606440.
[8] Mirshekari B, Zarei-Hanzaki A, Barabi A, Moshiri A, Abedi HR, Lee S-J, et al. Optimizing the austenite stability in a ferritic lightweight steel through thermomechanical processing.

Mater Charact 2020;166:110367. https://doi.org/10.1016/j.matchar.2020.110367.
[9] Sohn SS, Choi K, Kwak J-H, Kim NJ, Lee S. Novel ferrite–austenite duplex lightweight steel with 77% ductility by transformation induced plasticity and twinning induced plasticity mechanisms. Acta Mater 2014;78:181–9. https://doi.org/10.1016/j.actamat.2014.06.059.
[10] Lee SJ, Park TM, Nam JH, Choi WS, Sun Y, Fujii H, et al. The unexpected stress-strain response of medium Mn steel after friction stir welding. Mater Sci Eng A 2019;744:340–8. https://doi.org/10.1016/j.msea.2018.12.041.
[11] Park S-J, Hwang B, Lee KH, Lee T-H, Suh D-W, Han HN. Microstructure and tensile behavior of duplex low-density steel containing 5mass% aluminum. Scripta Mater 2013;68:365–9. https://doi.org/10.1016/j.scriptamat.2012.09.030.
[12] Lee K, Park SJ, Choi YS, Kim SJ, Lee TH, Oh KH, et al. Dual-scale correlation of mechanical behavior in duplex low-density steel. Scripta Mater 2013;69:618–21. https://doi.org/10.1016/j.scriptamat.2013.07.015.
[13] Differt K, Esmann U, Mughrabi H. A model of extrusions and intrusions in fatigued metals II. Surface roughening by random irreversible slip. Philos Mag A 1986;54:237–58. https://doi.org/10.1080/01418618608242897.
[14] Mughrabi H. Cyclic slip irreversibilities and the evolution of fatigue damage. Metall Mater Trans A 2009;40:1257–79. https://doi.org/10.1007/s11661-009-9839-8.
[15] Mughrabi H. Cyclic slip irreversibility and fatigue life: a microstructure-based analysis. Acta Mater 2013;61:1197–203. https://doi.org/10.1016/j.actamat.2012.10.029.
[16] Mughrabi H. Microstructural fatigue mechanisms: cyclic slip irreversibility, crack initiation, non-linear elastic damage analysis. Int J Fatig 2013;57:2–8. https://doi.org/10.1016/j.ijfatigue.2012.06.007.
[17] Mughrabi H. Revisiting "steady-state" monotonic and cyclic deformation: emphasizing the quasi-stationary state of deformation. Metall Mater Trans A 2020;51:1441–56. https://doi.org/10.1007/s11661-019-05618-x.
[18] Rezaei M, Zarei-Hanzaki A, Anousheh AS, Abedi HR, Pahlevani F, Hossain R, et al. On the damage mechanisms during compressive dwell-fatigue of β-annealed Ti-6242S alloy. Int J Fatig 2021;146:106158. https://doi.org/10.1016/j.ijfatigue.2021.106158.
[19] Nikulin I, Sawaguchi T, Ogawa K, Tsuzaki K. Effect of γ to ε martensitic transformation on low-cycle fatigue behaviour and fatigue microstructure of Fe–15Mn–10Cr–8Ni–xSi austenitic alloys. Acta Mater 2016;105:207–18. https://doi.org/10.1016/j.actamat.2015.12.002.
[20] Vakili SM, Zarei-Hanzaki A, Anoushe AS, Abedi HR, Mohammad-Ebrahimi MH, Jaskari M, et al. Reversible dislocation movement, martensitic transformation and nano-twinning during elastic cyclic loading of a metastable high entropy alloy. Acta Mater 2020;185:474–92. https://doi.org/10.1016/j.actamat.2019.12.040.
[21] Anoushe AS, Zarei-Hanzaki A, Abedi HR, Barabi A, Huang C, Berto F. On the microstructure evolution during isothermal low cycle fatigue of β-annealed Ti-6242S titanium alloy: internal damage mechanism, substructure development and early globularization. Int J Fatig 2018;116:592–601. https://doi.org/10.1016/j.ijfatigue.2018.07.014.
[22] Moshiri A, Zarei-Hanzaki A, Anoushe AS, Abedi HR, Mirshekari B, Berto F. Stress-relaxation viewpoint to study the room-temperature cyclic deformation behavior of a low-density steel. Int J Fatig 2020;139:105673. https://doi.org/10.1016/j.ijfatigue.2020.105673.
[23] Akbarian S, Dehghani K. On the molecular dynamics simulation of fatigue behavior of pre-cracked aluminum chip for NEMS application: effect of cyclic loading mode and surface roughness geometry. Int J Fatig 2020;135:105570. https://doi.org/10.1016/j.ijfatigue.2020.105570.
[24] Nikulin I, Sawaguchi T, Kushibe A, Inoue Y, Otsuka H, Tsuzaki K. Effect of strain amplitude on the low-cycle fatigue behavior of a new Fe–15Mn–10Cr–8Ni–4Si seismic damping alloy. Int J Fatig 2016;88:132–41. https://doi.org/10.1016/j.ijfatigue.2016.03.021.
[25] Laird C, Charsley P, Mughrabi H. Low energy dislocation structures produced by cyclic deformation. Mater Sci Eng, A 1986;81:433–50. https://doi.org/10.1016/0025-5416(86)90281-8.
[26] Li H, Koyama M, Sawaguchi T, Tsuzaki K, Noguchi H. Importance of crack-propagation-induced ε-martensite in strain-controlled low-cycle fatigue of high-Mn austenitic steel. Phil Mag Lett 2015;95:303–11. https://doi.org/10.1080/09500839.2015.1052029.
[27] Sawaguchi T, Nikulin I, Ogawa K, Sekido K, Takamori S, Maruyama T, et al. Designing Fe–Mn–Si alloys with improved low-cycle fatigue lives. Scripta Mater 2015;99:49–52. https://doi.org/10.1016/j.scriptamat.2014.11.024.
[28] Nandy S, Sekhar AP, Kar T, Ray KK, Das D. Influence of ageing on the low cycle fatigue behaviour of an Al–Mg–Si alloy. Philos Mag 2017;97:1978–2003. https://doi.org/10.1080/14786435.2017.1322729.
[29] BACHE M. A review of dwell sensitive fatigue in titanium alloys: the role of microstructure, texture and operating conditions. Int J Fatig 2003;25:1079–87. https://doi.org/10.1016/S0142-1123(03)00145-2.
[30] Goswami T. Low cycle fatigue—dwell effects and damage mechanisms. Int J Fatig 1999;21:55–76. https://doi.org/10.1016/S0142-1123(98)00056-5.
[31] Goswami T, Hänninen H. Dwell effects on high temperature fatigue behavior. Mater Des 2001;22:199–215. https://doi.org/10.1016/S0261-3069(00)00060-1.
[32] Curtze S, Kuokkala V-T, Oikari A, Talonen J, Hänninen H. Thermodynamic modeling of the stacking fault energy of austenitic steels. Acta Mater 2011;59:1068–76. https://doi.org/10.1016/j.actamat.2010.10.037.
[33] Saeed-Akbari A, Imlau J, Prahl U, Bleck W. Derivation and variation in composition-dependent stacking fault energy maps based on subregular solution model in high-manganese steels. Metall Mater Trans A 2009;40:3076–90. https://doi.org/10.1007/s11661-009-0050-8.
[34] ASTM E8. ASTM E8/E8M standard test methods for tension testing of metallic materials. Annu Book ASTM Stand 2010;4:1–27. https://doi.org/10.1520/E0008.
[35] ASTM. In: Standard test method for strain-controlled fatigue testing, vol. 96; 2004. https://doi.org/10.1520/E0606-04E01.
[36] Wang YM, Ma E. Strain hardening, strain rate sensitivity, and ductility of nanostructured metals. Mater Sci Eng A 2004;375–377:46–52. https://doi.org/10.1016/j.msea.2003.10.214.
[37] Abedi HR, Zarei Hanzaki A, Nemati N, Kim D-E. Trading off between dynamic strain aging and substructure evolution in κ-carbide-free lightweight steel at room temperature. Scripta Mater 2018;157:110–4. https://doi.org/10.1016/j.scriptamat.2018.07.044.
[38] Hörnqvist M, Karlsson B. Influence of heat treatment on the cyclic deformation properties of aluminium alloy AA7030. Mater Sci Eng A 2008;479:345–55. https://doi.org/10.1016/j.msea.2007.06.078.

[39] Lu L, Zhu T, Shen Y, Dao M, Lu K, Suresh S. Stress relaxation and the structure size-dependence of plastic deformation in nanotwinned copper. Acta Mater 2009;57:5165–73. https://doi.org/10.1016/j.actamat.2009.07.018.
[40] De Cooman BC, Estrin Y, Kim SK. Twinning-induced plasticity (TWIP) steels. Acta Mater 2018;142:283–362. https://doi.org/10.1016/j.actamat.2017.06.046.
[41] Laplanche G, Bonneville J, Varvenne C, Curtin WA, George EP. Thermal activation parameters of plastic flow reveal deformation mechanisms in the CrMnFeCoNi high-entropy alloy. Acta Mater 2018;143:257–64. https://doi.org/10.1016/j.actamat.2017.10.014.
[42] Hong S. The tensile and low-cycle fatigue behavior of cold worked 316L stainless steel: influence of dynamic strain aging. Int J Fatig 2004;26:899–910. https://doi.org/10.1016/j.ijfatigue.2003.12.002.
[43] Hong S-G, Lee S-B. Dynamic strain aging under tensile and LCF loading conditions, and their comparison in cold worked 316L stainless steel. J Nucl Mater 2004;328:232–42. https://doi.org/10.1016/j.jnucmat.2004.04.331.
[44] Hong S-G, Lee S-B. Mechanism of dynamic strain aging and characterization of its effect on the low-cycle fatigue behavior in type 316L stainless steel. J Nucl Mater 2005;340:307–14. https://doi.org/10.1016/j.jnucmat.2004.12.012.
[45] Rao KBS, Valsan M, Sandhya R, Mannan SL, Rodriguez P. Dynamic strain ageing effects in low cycle fatigue. High Temp Mater Process 1986;7:171–8. https://doi.org/10.1515/HTMP.1986.7.2-3.171.
[46] Cai ZH, Ding H, Misra RDK, Ying ZY. Austenite stability and deformation behavior in a cold-rolled transformation-induced plasticity steel with medium manganese content. Acta Mater 2015;84:229–36. https://doi.org/10.1016/j.actamat.2014.10.052.
[47] Sevsek S, Brasche F, Haase C, Bleck W. Combined deformation twinning and short-range ordering causes serrated flow in high-manganese steels. Mater Sci Eng A 2019;746:434–42. https://doi.org/10.1016/j.msea.2019.01.042.
[48] Mughrabi H. Microstructural mechanisms of cyclic deformation, fatigue crack initiation and early crack growth. Philos Trans R Soc A Math Phys Eng Sci 2015;373:20140132. https://doi.org/10.1098/rsta.2014.0132.
[49] Caillard D, Martin J-L. Thermally activated mechanisms in crystal plasticity. Elsevier; 2003.
[50] Orowan E. Problems of plastic gliding. Proc Phys Soc 1940;52:8–22. https://doi.org/10.1088/0959-5309/52/1/303.
[51] Liu G, Salvat Cantó J, Winwood S, Rhodes K, Birosca S. The effects of microstructure and microtexture generated during solidification on deformation micromechanism in IN713C nickel-based superalloy. Acta Mater 2018;148:391–406. https://doi.org/10.1016/j.actamat.2018.01.062.
[52] Tchoufang Tchuindjang J, Lecomte-Beckers J. Fractography survey on high cycle fatigue failure: crack origin characterisation and correlations between mechanical tests and microstructure in Fe–C–Cr–Mo–X alloys. Int J Fatig 2007;29:713–28. https://doi.org/10.1016/j.ijfatigue.2006.06.012.
[53] Nezhadfar PD, Shrestha R, Phan N, Shamsaei N. Fatigue behavior of additively manufactured 17-4 PH stainless steel: synergistic effects of surface roughness and heat treatment. Int J Fatig 2019;124:188–204. https://doi.org/10.1016/j.ijfatigue.2019.02.039.
[54] Nezhadfar PD, Anderson-Wedge K, Daniewicz SR, Phan N, Shao S, Shamsaei N. Improved high cycle fatigue performance of additively manufactured 17-4 PH stainless steel via in-process refining micro-/defect-structure. Addit Manuf 2020;36:101604. https://doi.org/10.1016/j.addma.2020.101604.
[55] Nezhadfar PD, Shamsaei N, Phan N. Enhancing ductility and fatigue strength of additively manufactured metallic materials by preheating the build platform. Fatig Fract Eng Mater Struct 2021;44:257–70. https://doi.org/10.1111/ffe.13372.
[56] Razavi SMJ, Ferro P, Berto F, Torgersen J. Fatigue strength of blunt V-notched specimens produced by selective laser melting of Ti-6Al-4V. Theor Appl Fract Mech 2018;97:376–84. https://doi.org/10.1016/j.tafmec.2017.06.021.
[57] Panin AV, Kazachenok MS, Panin SV, Berto F. Scale levels of quasi-static and dynamic fracture behavior of Ti-6Al-4V parts built by various additive manufacturing methods. Theor Appl Fract Mech 2020;110:102781. https://doi.org/10.1016/j.tafmec.2020.102781.
[58] Khosravani MR, Berto F, Ayatollahi MR, Reinicke T. Fracture behavior of additively manufactured components: a review. Theor Appl Fract Mech 2020;109:102763. https://doi.org/10.1016/j.tafmec.2020.102763.
[59] Song W, Liu X, Berto F, Razavi SMJ. Low-cycle fatigue behavior of 10CrNi3MoV high strength steel and its undermatched welds. Materials (Basel) 2018;11:661. https://doi.org/10.3390/ma11050661.
[60] Lenets Y. Crack propagation life prediction for Ti-6Al-4V based on striation spacing measurements. Int J Fatig 2000;22:521–9. https://doi.org/10.1016/S0142-1123(00)00019-0.
[61] Huang Z, Wagner D, Bathias C. Some metallurgical aspects of dynamic strain aging effect on the low cycle fatigue behavior of C–Mn steels. Int J Fatig 2015;80:113–20. https://doi.org/10.1016/j.ijfatigue.2015.04.008.
[62] Pham MS, Solenthaler C, Janssens KGF, Holdsworth SR. Dislocation structure evolution and its effects on cyclic deformation response of AISI 316L stainless steel. Mater Sci Eng A 2011;528:3261–9. https://doi.org/10.1016/j.msea.2011.01.015.
[63] Heczko M, Polák J, Kruml T. Microstructure and dislocation arrangements in Sanicro 25 steel fatigued at ambient and elevated temperatures. Mater Sci Eng A 2017;680:168–81. https://doi.org/10.1016/j.msea.2016.10.076.
[64] Karlsen W, Ivanchenko M, Ehrnstén U, Yagodzinskyy Y, Hänninen H. Microstructural manifestation of dynamic strain aging in AISI 316 stainless steel. J Nucl Mater 2009;395:156–61. https://doi.org/10.1016/j.jnucmat.2009.10.047.
[65] Xie R, Lu S, Li W, Tian Y, Vitos L. Dissociated dislocation-mediated carbon transport and diffusion in austenitic iron. Acta Mater 2020;191:43–50. https://doi.org/10.1016/j.actamat.2020.03.042.
[66] Zhou H, Zhang H, Bai F, Song M, Chen Y, Zhang L, et al. Planar dislocation structure during creep-fatigue interactions of TP347H heat-resistant austenitic steel at 600 °C. Mater Sci Eng A 2020;779:139141. https://doi.org/10.1016/j.msea.2020.139141.
[67] Koyama M, Sawaguchi T, Tsuzaki K. Deformation twinning behavior of twinning-induced plasticity steels with different carbon concentrations – Part 2: proposal of dynamic-strain-aging-assisted deformation twinning. ISIJ Int 2015;55:1754–61. https://doi.org/10.2355/isijinternational.ISIJINT-2015-070.
[68] Abedi HR, Hanzaki AZ, Haghdadi N, Hodgson PD. Substructure induced twinning in low density steel. Scripta Mater 2017;128:69–73. https://doi.org/10.1016/j.scriptamat.2016.10.001.
[69] Sauzay M, Kubin LP. Scaling laws for dislocation microstructures in monotonic and cyclic deformation of fcc metals. Prog Mater Sci 2011;56:725–84. https://doi.org/10.1016/j.pmatsci.2011.01.006.
[70] Sangid MD. The physics of fatigue crack initiation. Int J Fatig 2013;57:58–72. https://doi.org/10.1016/j.ijfatigue.2012.10.009.